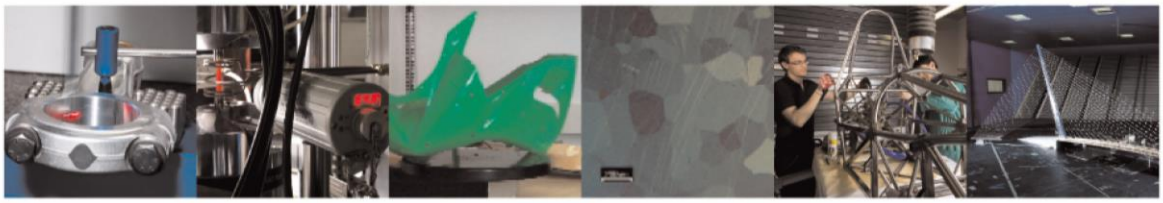

Design and Implementation of a Multisensor Coaxial Monitoring System With Correction Strategies for Selective Laser Melting of a Maraging Steel

Gökhan Demir, Ali; De Giorgi, Chiara; Previtali, Barbara

This is a post-peer-review, pre-copyedit version of an article published in JOURNAL OF MANUFACTURING SCIENCE AND ENGINEERING, 140/4, on February 5, 2018. The final authenticated version is available online at: http://dx.doi.org/10.1115/1.4038568

https://asmedigitalcollection.asme.org/manufacturingscience/article/doi/10.1115/1.4038568/380512/Design-and-Implementation-of-a-Multisensor-Coaxial

DIPARTIMENTO DI MECCANICA ■ POLITECNICO DI MILANO
via G. La Masa, 1 ■ 20156 Milano ■ EMAIL (PEC): pecmecc@cert.polimi.it
http://www.mecc.polimi.it
Rev. 0

Design and implementation of a multi-sensor coaxial monitoring system with correction strategies for selective laser melting of a maraging steel

Ali Gökhan Demir[1]
Department of Mechanical Engineering, Politecnico di Milano
Via La Masa 1, 20156 Milan, Italy
aligokhan.demir@polimi.it

Chiara De Giorgi
Department of Mechanical Engineering, Politecnico di Milano
Via La Masa 1, 20156 Milan, Italy
chiara.degiorgi@polimi.it

Barbara Previtali
Department of Mechanical Engineering, Politecnico di Milano
Via La Masa 1, 20156 Milan, Italy
barbara.previtali@polimi.it

ABSTRACT

Development of monitoring devices becomes crucially important in selective laser melting due to the high process complexity and the high value of the products obtained. This work discusses the design of a coaxial monitoring system for SLM using multiple sensors. In particular, an optical model is developed for the propagation of the process emission from the workpiece to the monitoring module. The model is used to determine the field of view around the monitored zone. The lens arrangements and the optical filters are chosen according to the model results. They were implemented to construct a monitoring module consisting of two CCD cameras viewing visible and near-infrared wavelength bands, as well as a photodiode viewing the back-reflected laser emission, all integrated in a coaxial configuration. The system

[1] Corresponding author information can be added as a footnote.

functionality is tested with a prototype SLM machine during the processing of 18Ni300 maraging steel, a material known to be prone to porosity. In particular, different remelting strategies were employed as possible correction strategies to reduce porosity. The signals were interpreted as being indicators of the change in absorptivity of the laser light by the powder bed, of the plasma and molten pool, as well as of the evolution of the temperature field.

Keywords: *Additive manufacturing; in-situ monitoring; defect correction; maraging steel*

INTRODUCTION

Additive manufacturing with metals has reached industrial maturity in the last decade. These processes are employed in several sectors such as medical, energy, aerospace, and tooling. Each of these sectors exploit different advantages provided by the processes such as geometrical flexibility, absence of tools and fixtures, and reduced time between design and production. Among different methods, powder-bed fusion (PBF) processes provide higher dimensional accuracy and increased feature resolution. Selective laser melting (SLM) belongs to this family of processes, where a high intensity laser beam is used to selectively fuse the metallic powder in a layer-by-layer fashion. The process resembles a more conventional laser welding process, inheriting all related defects [1], yet it is applied in a much longer track. In a volume of 1 cm^3, the total length of the scanned tracks exceeds 3 km. Defect formation has a high probability due to this scale factor during the melting process itself. Porosity, which is mainly due to molten track formation and solidification, is still one of the major problems of the SLM process [2, 3]. While SLM produced components match the performance of wrought counterparts under static loads, even a small fraction of porosity could reduce mechanical fatigue properties drastically [4]. Moreover, process drifts may occur over

time mainly due to the thermal load on the build piece. Resultantly, cracking and thermal deformations may occur [5, 6]. A feature of the powder-bed fusion processes is that several different parts can be manufactured on the same building plate. This generates a distinct problem, i.e. catastrophic failure of the whole build due to the defect formation in a single component. Powder-bed stability is an important factor, where recoater wear and detachment of debris can result in propagating the defect over other built parts.

Online process monitoring in SLM is crucially important for both small lot and highly customized parts, as well as mass production of highly complex components [7]. The first scenario better applies to components with rapid design changes (e.g. motorsports, tool making, and custom implant manufacturing), where the component value is high and the time between design and production is important. The second scenario applies to an established production (e.g. aviation and energy), where process drifts and changes in production lots are carefully assessed for certification. With the growing demand, monitoring needs become relevant at an industry level [8]. Several monitoring techniques have been proposed in the literature for additive manufacturing of metals [9, 10], whereas the specific works on selective laser melting are limited. Coaxial arrangement was preferred by different groups, where the sensor is placed between the scan head and the laser source. This way, the sensor follows the position of the laser beam throughout the process. Kruth's group has carried out the pioneering works in the field employing coaxial monitoring with high speed cameras and photodiodes on stainless steel and titanium alloys [11–15]. They have developed a feed-

back control using the photodiode signal observing the visible bandwidth and acting over the laser power [16]. On a coaxial configuration, interferometric imaging has also been applied mainly to investigate the molten pool height [17] during the SLM of stainless steel and powder-bed regularity [18]. The use of coaxial pyrometer has also been demonstrated with stainless steel [19]. The use of coaxial configuration can be limiting for some sensors due to the scarce transmissivity of the existing optical chain and it does not allow to capture the image of the whole powder bed. Several works report the use off-axis configuration in literature. The state of the powder bed has been monitored after each layer by an off-axis camera during the SLM of Inconel 625 [20]. Thermal imaging has been applied to monitor the heat induced deformations on the overall geometry with Inconel 718 [21]. Furumoto et al. employed pyrometry for measuring surface temperature during the process [22]. Yadroitsev et al. employed a coaxial CCD camera for estimating the temperature during the SLM of Ti6Al4V alloy [23]. Spark detection with high speed imaging has also been proposed depicting material loss and overheating regions [24, 25]. Matthews et al. employed high speed imaging with external illumination in an off-axis configuration to detect the formation of denudation phenomenon of Ti6Al4V powder [26]. The use of multiple sensors from an off-axis perspective with high speed imaging has also been proposed [27]. Another proposed method has been spectrometry, improving the wavelength resolution of the acquired signal [28, 29]. Most of these works have identified process fingerprints over the analysed signals depicting the instabilities. Commonly, the research groups have focused on the defect formation on either the single track or on the different layers

using continuous wave laser sources. The choice of the monitoring sensor and its implementation should be suitable for carrying out the monitoring task throughout the whole build.

Another important point is that, downstream the monitoring scheme, correction strategies should be developed and employed downstream the monitoring scheme. Corrective measures can be more effective than online control schemes in the case of defects that form in a very short duration of time (e.g. porosity). Layer remelting is a non-invasive and simple option for porosity correction [30]. However, remelting every single layer comes intrinsically with a longer production time. Applying the corrective measure would be more feasible layer-wise where needed. In an ideal case, the defect formation could be identified as a function of the scanned position and the corrective remelting can be applied only on this position.

The overall analysis shows there is an evident lack of information regarding the monitoring of SLM process applied with pulsed wave lasers. Moreover, the methods have been applied to materials known to be processed well with the SLM process, whereas materials with low processability such as maraging steel, have not been studied. Moreover, to authors' knowledge, none of the previous works report the use of correction strategies along with the monitoring method analysing their efficacy on the related defect.

Accordingly, this work proposes a multi-sensor monitoring scheme with coaxial configuration for SLM, which observes process emission and back-reflected laser light. The paper describes the design criteria based on the link with the process physics and

optical configuration required to determine the field of view. With the construction of a flexible monitoring system consisting of multiple sensors, different transitory behaviour in the process are viewed providing both a better comprehension of the process and means for signalling the defect formation. In particular, the signal behaviour is sought to be related to the porosity formation. The developed module is implemented and used in the pulsed wave SLM of 18Ni300 maraging steel, which is known to possess low processabilityde[31]. This material is used in highly demanding applications such as tooling, automotive, and aerospace, where quality requirements are highly restringing. Hence, it fundamental to develop and apply process monitoring and correction strategies. Correction strategies based on remelting are applied to test their effect on the reduction of part porosity.

MONITORING MODULE DESIGN

Choice of observed bandwidths

The monitoring module was divided in three channels to follow different phenomenon occurring simultaneously. The channel division was based on wavelength band choice, hence constituting the overall wavelength resolution of the system. Indeed, such division is much more limited compared to a spectroscope. Key physical phenomenon occurring during the process generate the sources of electromagnetic radiation [32], and can be divided in main bands, providing a compromise between spatial, temporal, and wavelength resolution requirements [33]. The process involves the absorption of the laser beam by the powder bed, which then heats and generates

the melt pool and possibly form keyhole [34]. The melt pool then can partially vaporize, generate spark, spatter, and plume. The sparks and vapour cause material loss and melt-pool instability [35]. The metallic vapour can absorb the laser beam obstructing its passage and eventually partially ionize [36, 37]. In an ideally stable process, laser absorption should be constant, melt pool and thermal field should be stable, excessive vapour and plume is avoided, and sparks are absent.

Table 1 reports the investigated physical phenomenon through the flexible monitoring system and the related physical references. The physical references are required to estimate the spatial and temporal resolutions required. The laser absorption can be indirectly sensed by monitoring the state of the back-reflected laser beam intensity. Therefore, one channel has been dedicated to the laser wavelength (1070 nm). The temporal resolution of the channel should suit the variations within the pulse duration for PW emission. Thus, high temporal resolution is required. The phenomenon should occur around the laser spot, which is related to the spatial resolution requirements. Electromagnetic emission due to plasma formation, plume and keyhole dynamics can be found in the visible region, which is a strong indicator to the melt pool stability and can be linked to the porosity formation [34, 38, 39]. Therefore, the third channel was implemented around 350 and 700 nm. The small fractions of pores remaining in the SLM built part under stable conditions are small and around 50-200 μm in diameter. Larger and interconnected pores between consecutive layers can form especially under insufficient melting conditions, which may have dimensions much larger than 200 μm. The observed region with the monitoring system should suit the

extent of the molten pool size. Pore formation should require the unstable melting conditions that take up to several laser pulses within a scan line, which can be used as the physical reference for the phenomenon. The thermal field is observable at infrared region. However, the transmissivity of the optical setup above laser wavelength is very low, which limits the implementation of a thermal camera. Instead, the near infrared (NIR) region falling between the visible and laser wavelengths can be used to trace the thermal radiation around the molten pool. Hence, a second channel was dedicated to near infrared region (900-1000 nm). Most of the digital CCD and CMOS cameras exhibit sufficient sensitivity around this bandwidth allowing for implementation of this choice easily. The thermal instabilities usually manifest between consecutive layers in the form of deformations as they depend on the geometry and the mass of the component. In order to form notable contractions between powder/solid/liquid metal interfaces more than a scanned track would be required, which is related to the spatial scale.

The theoretical modelling principles discussed here are mainly based on the geometrical optics theories [40]. The total magnification (m_{tot}) of an optical system depends on the basic relationship between the field of view (FOV) and the image size, or in the present case the size of the sensor (d_{sensor}). The total magnification can be calculated as follows.

$$m_{tot} = \frac{d_{sensor}}{FOV} \quad (1)$$

Eq.1 depicts that for a given sensor, in order to achieve a desired field of view, the total magnification should be fulfilled. Figure 1.a depicts a generic optical system composed of three lenses. For the given system distance from a lens to the object is

referred as *q*, whereas distance from the lens to an image field is *p*. For a generic system composed of *M* lenses, the total magnification can be calculated as follows.

$$m_{tot} = \prod_{i=1}^{M} -\frac{q_i}{p_i} \quad (2)$$

On the other hand, for each lens, thin lens equation should be applied, where

$$\frac{1}{f_i} = \frac{1}{p_i} + \frac{1}{q_i} \quad (3)$$

with

$$p_{i+1} = d_i - q_i \quad (4)$$

Figure 1.b depicts the optical arrangement of a monitoring module inserted in an SLM system with an existing f-theta lens. A three-lens configuration composed of 2 positive and a negative lens is proposed in order to decrease to the total length of the optical path. For the given system, Eq.3 and 4 can be rewritten as follows.

$$\begin{cases} \frac{1}{f_0} = \frac{1}{p_0} + \frac{1}{q_0} \\ \frac{1}{f_1} = \frac{1}{d_2 - q_1} + \frac{1}{q_1} \\ \frac{1}{f_2} = \frac{1}{d_2 - q_2} + \frac{1}{q_1} \\ \frac{1}{f_3} = \frac{1}{d_3 - q_2} + \frac{1}{q_3} \end{cases} \quad (5)$$

$$m_{tot} = \left(\frac{q_0}{p_0}\right)\left(\frac{q_1}{d_1 - q_0}\right)\left(\frac{q_2}{d_2 - q_1}\right)\left(\frac{q_3}{d_3 - q_2}\right) \quad (6)$$

It should be noted that p_0 and d_1 refer to the distances related to the equivalent f-theta lens, whereas f_0 is the back focal length of the equivalent f-theta lens. These dimensions rely on the technological choices, which are the optical arrangements provided for the laser propagation. Therefore, they are the initial constraints of the design. Both p_0 and f_0 should be characterized prior to the calculations for the given

machine configuration. Focal lenses are chosen as a function of the desired field of view as well as the available space for the module. Model outputs are d_3 and d_4 and are a function of the optical components of the machine, sensor size, and the chosen lenses. It should be noted that the model does not take the system aberrations into account.

EXPERIMENTAL

Material

Throughout the study 18Ni300 maraging steel powder was used (Sandvik Osprey, Neath, UK). The powder was atomized in nitrogen and characterized by a spherical shape. Average particle size was 32 μm and with 5 g/cm^3 tap density. Nominal material density was 8.1 g/cm^3 [41]. The material is known to produce sparks and possess low processability with SLM [31]. Despite constituting a critical case for SLM process stability, process monitoring and consecutive correction strategies on this material have not been investigated before.

SLM system with coaxial monitoring module

A prototype SLM system, namely Powderful, was used throughout the study, allowing flexible control over the whole process parameters. The laser source was a single mode fibre laser with 250 W maximum power (IPG Photonics YLR-150/750-QCW-AC, Cambridge, MA, USA). The laser beam was collimated with a 50 mm focal lens and launched into a zoom optic (VarioScan 20 from Scanlab, Puchheim, Germany) to regulate the beam focal plane, which than was manipulated and focused by the scanner

head (HurryScan 14 from Scanlab, Puchheim, Germany). The scan path trajectory was designed using Scanmaster software (Cambridge Technologies, Bedford, MA, USA). The scanner housed a 420 mm f-theta lens. In this configuration, the beam diameter at the focal plane (d_0) was calculated as 60 µm. The main specifications of the laser system are summarized in Table 2. The powder deposition system was in-house designed and produced [42]. The control of the system and monitoring of the machine state was carried out in LabVIEW environment (National Instruments, Austin, TX, USA). The system allowed to operate in a controlled processing chamber under process gas. Vacuum was applied down to 50 mbar pressure first and then process gas was flooded. This procedure was repeated 3 times.

The system was operated with PW emission. The majority of the industrial SLM systems operate with CW emission, whereas further attention is required on the monitoring of the process as pulsed emission yields differences in the molten pool formation and stability [43]. In particular, the laser is positioned on a certain spot to emit with a given peak power (P_{peak}) for a fixed pulse duration (t_{on}) in µs range. The laser jumps onto the consecutive spot on the scanned line and applies the exposure. At the end of each scanned line, the laser jumps to the adjacent one. The operation is continued until the layer is scanned completely.

Five main process parameters have been identified for the study. Laser power controls pulse peak power (P_{peak}). Pulse duration controls the duration of the laser pulse applied to each spot on the scanned line and corresponds to t_{on}. The point distance between consecutive laser spots on a scan line (d_p) and the hatch distance between the

adjacent scan lines (d_h) are also controlled to vary the energy released on the powder bed.

A coaxial monitoring system was implemented on the open architecture of the machine. Figure 2.a shows a schematic description of the monitoring module. A FOV of 1x1 mm^2 was chosen as it provided sufficient spatial resolution to all the sensors for observing the listed phenomenon. The sensor choice was a compromise between the overall requirements. Off-the-shelf and low-cost sensors were preferred for an easier implementation on the existing industrial systems. Three channels were implemented observing visible (350-700 nm), near infrared (NIR, 700-1000 nm), and laser emission (1064$\pm$10 nm) bandwidths. For visible and near infrared channels, spatial resolutions were aimed to be preserved, whereas for the laser channel temporal resolution had to be favoured. The process emission was intercepted via a dichroic mirror implemented before the galvanometric mirrors of the scanner head. The process light was then split into different channels using beam splitters and consecutively filtered by optical filters to select the desired wavelength bands. A CCD camera was employed for the visible channel with a 1288x964 resolution and 3.75 µm pixel size (Flea3 from Point Grey Research, Richmond, BC, Canada). For the NIR channel a CMOS camera with 2592x1933 resolution and 2.2 µm pixel size (acA2500-14gm from Basler Ahrensburg, Germany). This camera provided sufficient sensitivity for the acquisition of the bandwidth, since quantum efficiency between 900 and 1000 nm is around 6%. Both cameras were run at a 68 fps acquisition rate and the sensor active area was reduced to 1.2x1.2 mm^2 in order to observe the desired FOV. Back reflected laser light was acquired with a fast

photodiode (SM05PD5A from Thorlabs, Newton, NJ, USA). Optical fiber delivery was used to transmit the back reflected laser light from the module to the photodiode. In particular, a three-lens configuration was implemented before the cameras in order to control the field of view. System components, in particular the three lenses (f_1, f_2, f_3) were chosen in order to achieve a 1x1 mm^2 field of view. Table 3 reports the final dimensions of the monitoring module according to the optical scheme expressed in Figure 1.b. The model was validated before experimentation by imaging a graduated artefact. Figure 2.b shows the implemented system.

Experimental plan

The experimental study was aimed at identifying the process transitories regarding laser absorption and thermal stability, and porosity formation. Correction strategies were applied together to investigate the efficacy of the method as well as the change in signal behaviour. As correction strategies, layer remelting is proposed using different process parameters. In this preliminary analysis, experimented conditions are evaluated layer-wise for simplicity.

SLM was applied with pulsed wave emission employing a point-by-point scan strategy. The laser jumped to the consecutive position after applying the desired pulse duration. In the experimental plan, the effect of pulse energy and different correction strategies based on remelting were tested. Cubic specimens with 5x5x5 mm^3 volume were produced. The scan trajectories were placed around the central portion of the f-theta lens to limit aberrations. The details of the experimental campaign are shown in

Table 4. Different pulse durations were tested without and with the use of remelting strategies namely, polishing, soft melting, and double pass. The parameters corresponding to the different remelting strategies are shown in Table 5. In the same table, the total amount of energy (E_{tot}) released by the end of the remelting passes over an area of 5x5 mm^2 is expressed for comparison, which is calculated using the following expression.

$$E_{tot} = \sum_{g=1}^{2} t_{on,g} P_{peak,g} \frac{l_1 l_2}{d_{p,g} d_{h,g}} \quad (7)$$

where l_1 and l_2 refer to the length and width of the scanner area.

Another important factor regarding the use of the correction strategies is the change in productivity. Build rate (*BR*) can be estimated by the following equation.

$$BR = \frac{1}{\sum_{g=1}^{2} \frac{t_{on,g}}{d_{p,g} d_{h,g} z}} \quad (8)$$

The formula takes only the laser emission time into account, where the durations between consecutive jumps, powder dosing and recoating are neglected. On the other hand, it is an effective way for understanding the impact of adding the remelting pass. Table 6 exhibits the calculated build rates for each tested condition.

All monitoring signals were acquired contemporarily. Laser channel was acquired using an oscilloscope at a 1 MHz sampling rate (TDS5034B from Tektronix, Oregon, USA). The acquisitions of the two cameras was carried out with a personal computer. Initially signals were analysed qualitatively to demonstrate the basic changes in the dynamics. During a second phase, the mean intensity of each channel was evaluated as a function

of scanned layer number (N_l). No post-processing was applied at this initial stage. The mean intensity of the photodiode signal for a given scanned layer was calculated as

$$I_{PD} = \frac{1}{j}\sum_{i=1}^{p} I_i \quad (9)$$

where j is the number of points acquired in the photodiode signal and I_i is the intensity i^{th} point. On the other hand, the mean intensity of the camera images for a given layer was calculated as

$$I_C = \frac{1}{k}\sum_{i=1}^{l} I_i \quad (10)$$

where k is the total number of frames and I_i is the intensity of i^{th} image, which is calculated as

$$I_i = \sum_{m=1}^{r}\sum_{n=1}^{c} I_{i_{m,n}} \quad (11)$$

where m and n are the indexes of the pixel row and column, for $r \times c$ number of pixels. Specimen density was evaluated with the Archimedes method using a high precision balance (Precisa 100A-300M, Turin, Italy).

RESULTS

Part density

Figure 3 reports the generated specimens. Figure 4 reports the porosity measurements as a function of pulse duration and remelting strategy. It can be seen that the part porosity levels vary between 1.2 and 1.8% for processing conditions without any remelting. The best remelting strategy appears to be the so-called polishing (*P*), where porosity is lowered down to 1% in average. Double pass (*DP*) and soft remelting (*SR*) show

improved porosity overall but increase variability with higher levels of pulse duration (t_{on}). Evidently, the use of higher total energy is useful for a complete melting of the layer by closing the formed pores over the first pass. The efficacy of the polishing strategy can be attributed to the use of a defocused beam able to reduce the heat penetration over the thickness and increase the molten pool width. Moreover, the resultant re-molten surface is overall flatter, which contributes to reduce porosity propagation over the layers [3]. It is worthwhile to note that the polishing strategy provides higher overall build rates among the remelting strategies. However, the use of the correction strategy on demand is the ideal solution.

Signal and image characteristics

A key advantage of the proposed multi-sensor monitoring system is that different physical phenomena can be observed via different channels, providing rich monitoring possibilities. Figure 5.a depicts the photodiode signal recorded through the laser channel (1064±10 nm). The signal mainly shows the change in reflectivity between consecutive volume and remelting passes. As shown in the zoomed part of the signal in Figure 5.b, the fast photodiode is capable of temporally resolving the laser pulses. In terms of a more detailed analysis, the laser channel can be used to detect the pulse shape deformation compared to the incoming one [44]. This way the pulse shape can be studied and tailored for purpose.

Figure 6 shows example images and the overall signal intensity as a function of frame number observed through the visible channel (400-700 nm). As shown in Figure

6.a, melt pool instability results in the disappearance of the high intensity region and the formation of a dark image. In this case, high intensity zone enlarges and the circular halo loses symmetry. In Figure 6.b the overall image intensity is show as function of frame number. It can be seen that several instances with spark generation is present over a certain scanned layer. Spark generation is an indicator insufficient melting and material loss.

A characteristic behaviour of the near infrared channel is demonstrated in Figure 7. The graphs show the overall intensity behaviour between the volume and remelting passes. The signal shows a smaller range of variation compared to the visible channel, implying that the thermal field is more stable than the melt pool dynamics. The signal is a proxy of the process temperature. In addition to the increase in the mean value between different pulse durations, the remelting pass evidently appears with much lower intensity. This can be attributed to the change in material properties between the powder and the solid. Most importantly, the thermal conductivity and density will increase once the non-reversible transformation between powder-liquid-solid is fulfilled. The remelting passes indicate a much lower intensity, showing that surface overheating is avoided. The near infrared channel can be highly useful for overhang structures and sharp edges, where thermal accumulations can occur and generate defects other than porosity.

Evolution of signal intensity

Figure 8, Figure 9, and Figure 10 show the mean signal intensity belonging to each layer obtained at different processing conditions for laser, visible, and near infrared channels respectively. In the graphs, the first scans applied on the powder are referred as “volume”, whereas the second scans on the solidified metal is referred to as “remelting”. Mean values demonstrate the general trend between consecutive scans and layers as a function of processing conditions.

Concerning the back reflected laser light, it is observed that signal intensity follows an asymptotic decay in all cases as the layers proceed. The highest intensities are observed on the initial layers, implying that absorptivity is at its lowest around the first layers, where the bonding between the loose powder and substrate should be achieved. After the 8^{th} layer, signal intensity stabilized for all conditions. The stabilization of the signal strength can be attributed to the settlement of the effective layer thickness [45]. After laser melting, assuming a complete melting, the density of the solid metal will be higher than the powder apparent density. With constant mass and area, the resultant zone will be lower in height compared to the initial situation. At the consecutive layer, the deposited powder will have to fill in a total height comprised of the axis movement (layer thickness) and the void generated by the density change. With the present tap density of the powder, effective layer thickness reaches 55 µm by the second layer, and stabilizes around 65 µm between 6^{th} and 10^{th} layers. An increased effective layer thickness allows for a longer distance for laser light to propagate within the powder, and to be absorbed more [46]. On the other hand, no significant difference

between volume and remelting passes are observed apart from the soft-remelting (*SR*) condition. Indeed, the remelting pass of this strategy is applied with a lower laser power. Therefore, both the incoming and reflected laser intensities are lower compared to the volume pass.

Concerning the visible channel, the signal intensities show a variety of responses as a function of processing conditions and layer number. An evident difference between volume and remelting scans is present at each processing strategy. This is expected to be due to the changes in the material properties between the powder and the solid. Resultantly, plume and molten pool dynamics change. It can be observed in Figure 9 that the overall strength of the volume pass increases for the conditions corresponding to lower porosity. Figure 11.a shows the change in mean intensity over different layers as a function of total energy. It can be seen that a clear correlation between the two parameters exist. Figure 11.b depicts the relationship between the overall porosity and the signal strength at volume pass. The error bars represent the variability of the indicators over different layers. The trend shows that increased visible emission can be correlated to melt pool stability and a reduction of the porosity. Together with the previous observations, it can be deduced that visible channel can be potentially employed for detecting porosity as a function of intensity decay and separations from the melt pool region. The signal intensity at the remelting layer can be employed as an indicator to the successful implementation of the correction. The use of a defocused beam with the polishing strategy (*P*) is expected to

reduce the energy intensity over the irradiated area and apply a gentle remelting providing low emission at the remelting pass.

In the case of the near infrared channel (900-1000 nm) a clear trend is visible in all conditions showing an exponential decay and a significant difference between volume and remelting passes. The difference between the volume and remelting intensities can be linked to the change in the conduction properties of the powder and solid metal. Surface temperature is expected to be much higher due to reduced conduction between the powder and the previously deposited solid layer. Once solidified, during the remelting pass heat is conducted in a more efficient manner reducing the surface temperature. On the other hand, the signal intensity stabilizes around the 32nd layer at both volume and remelting passes. This is expected to be due to the formation of an equilibrium state, where the conduction and heating by the laser beam are balanced at a certain component volume. Reaching the equilibrium temperature depends on the deposited volume as well as the process parameters. The overall temperature of the build chamber also affects this condition. Having the same volume and being deposited together, the samples reach the equilibrium state at similar layers. The infrared channel can be further exploited to distinguish over- and under-heating conditions with large and small components built together.

DISCUSSION

The presented results underline the advantage of employing multiple sensors in the monitoring scheme during the SLM of a tool steel with low processability. The use of

a coaxial arrangement provides the possibility of observing the same position over the scanned track during the melting phenomenon. The employed sensors were deliberately chosen as off-the-shelf, low-cost commercial products. This provides high flexibility in implementation on existing systems and new ones. Another point relates to the data size. In terms of sensor choice, a compromise is required between temporal, spatial, and wavelength bandwidth resolutions. A single device capable of providing high resolution in all of the mentioned parameters is either highly costly or difficult to implement due to the very large amount of data acquired. Spectroscopes can be employed to resolve wavelength down to pm levels. However, without intense plasma formation, the acquisition of process emission with a spectroscope may require longer exposure times. Spatial resolution is intrinsically lost, unless multiple sensors are positioned. On the other hand, a fast photodiode provides high temporal resolution and a voltage signal easy to implement in an on-board analysis system. Accordingly, they found use different monitoring schemes in other laser-based manufacturing processes [16],[47]. Many of the temperature measurement systems based on pyrometers implement similar solutions. The compromise of higher temporal resolution over spatial resolution for back-reflected laser light is due to the importance of the overall change in material absorption. Implementing a camera instead of a photodiode could resolve the change in absorbance around the molten pool, which requires very high spatial resolution as well as a high dynamic range due to the very bright laser beam. In the present case, the spatial resolution on the powder bed plane (x, y) was maintained high by carefully implementing the optical components to achieve a limited field of view. The

images, especially in the case of the visible channel, show process dynamics, which cannot be easily resolved by intensity measurements. Measurements related to the plume and spark size can be exploited for defect detection as well as recognition of the cause. For instance, increased metallic vapour and spark can both generate porosity. While a decrease in laser power may be beneficial to reduce vaporization, sparks can be removed with a change in process gas flow rate [48]. Indeed, to separate the defect causes, more sophisticated image analysis techniques are required, which have not been the concern of the present work. Identification of the defect type and cause has an evident link to control and correction methods. Layer remelting is a straight-forward and non-intrusive approach to correcting porosity and possibly some of the geometrical errors. Subtractive approaches can be also implemented, especially concerning geometrical errors and surface roughness [49].

Finally, it should be noted that a multi-sensor approach can also benefit from the inclusion of off-axis instruments. As a matter of fact, some defects are generated in time scales much longer than the melting phenomenon and in dimensional scales much larger than the molten pool zone. These are mainly related to the regularity of the powder-bed and thermal deformations occurring during the cooling cycles.

CONCLUSIONS

This work presents the design criteria and the implementation of a coaxial monitoring scheme for pulsed wave selective laser melting. In particular, the system employed two digital cameras and a photodiode observing different wavelength bands

in the electromagnetic spectrum. The monitoring system was used during the pulsed wave SLM of 18Ni300 maraging steel, a material possessing low processability with PW laser emission. The present configuration represented a real industrial case in need of monitoring and correction solutions, which was assessed for the first time. The main conclusions of this work are as follows.

- The model for calculating the field of view provides a basic tool for choosing the correct optical elements for the monitoring module. The accuracy of the model was confirmed for stationary conditions working in the central area of the f-theta lens.
- Remelting strategies improve the part density of 18Ni300 components. The most effective one was found to be the so called polishing strategy based on superficial remelting.
- Back-reflected laser intensity changes significantly between different layers. A stable behaviour is observed once the effective layer thickness stabilizes. Signal intensity varies intrinsically as the laser power changes. Reflected pulse shape can be further useful for understanding the absorption phenomenon on a restricted time scale.
- The visible channel depicted the stability of the melt pool. The images show melt pool separation and excessive plume generation. The overall intensity could be linked to the porosity and can be further developed to depict changes at a layer level. The intensity difference between the volume and remelting passes can be exploited to confirm the success of the correction strategy.

- The near infrared channel showed asymptotic behaviour, reaching stability on a longer time scale. Evidently, the thermal equilibrium between heating by the laser beam, conduction and convection are balanced at a certain component volume, which corresponded to approximately the 32nd layer in the examined case.

Beyond the listed specific results, the work demonstrates the efficacy of the developed monitoring system with commercial and low-cost equipment. For a complete monitoring setup able to alarm at the defect formation, data analysis plays a fundamental role. This way, the provided correction strategies can be used on-demand and where required. Accordingly, future works will address improvement of the existing monitoring scheme in terms of optical correction of the aberrations in the optical field and in data analysis. The use of the same optical chain to observe the geometry of the molten pool by suppressing the process emission and using external illumination will be also evaluated.

ACKNOWLEDGMENT

Mr. Davide Beretta and Mr. Matteo Bozzani are gratefully acknowledged for their support in the experimental phase. The authors wish to express their gratitude to, BLM Group, IPG Photonics Italy, and Renishaw for their collaboration.

FUNDING

This work was supported by Regione Lombardia under the call “Creatività: Eventi e Luoghi per L’innovazione nella Moda e nel Design, Linea 2: Infrastrutturazione Fisica e Digitale”.

NOMENCLATURE

Δz	Focal position
BR	Build rate
c	Number of pixel columns
d	Distance between lenses
d_0	Nominal beam diameter on focal plane
d_h	Hatch distance
d_p	Point distance
DP	Double pass
d_{sensor}	Sensor size
E_{tot}	Total amount of energy
f	Focal length of a lens
FOV	Field of view
I	Intensity
I_C	Mean intensity of the camera images
I_{PD}	Mean intensity of the photodiode
j	Number of points acquired in the photodiode signal
k	Total number of frames
l_1	Length of the scanned area

l_2	Width of the scanned area
M^2	Beam quality factor
m_{tot}	Total magnification
N	No remelting (none)
N_l	Layer number
p	Distance from the lens to an image field
P	Polishing
P_{max}	Maximum laser power
P_{peak}	Peak power
q	Distance from a lens to the object
r	Number of pixel rows
SR	Soft remelting
t_{on}	Pulse duration
z	Layer thickness

REFERENCES

1. Kawahito Y, Mizutani M, Katayama S (2007) Elucidation of high-power fibre laser welding phenomena of stainless steel and effect of factors on weld geometry. J Phys D Appl Phys 40:5854–5859 . doi: 10.1088/0022-3727/40/19/009
2. Gong H, Rafi K, Gu H, et al (2014) Analysis of defect generation in Ti-6Al-4V parts made using powder bed fusion additive manufacturing processes. Addit Manuf 1:87–98 . doi: 10.1016/j.addma.2014.08.002
3. Qiu C, Panwisawas C, Ward M, et al (2015) On the role of melt flow into the surface structure and porosity development during selective laser melting. Acta Mater 96:72–79 . doi: 10.1016/j.actamat.2015.06.004
4. Song B, Zhao X, Li S, et al (2015) Differences in microstructure and properties between selective laser melting and traditional manufacturing for fabrication of metal parts: A review. Front Mech Eng 10:111–125 . doi: 10.1007/s11465-015-0341-2
5. Harrison NJ, Todd I, Mumtaz K (2015) Reduction of micro-cracking in nickel superalloys processed by Selective Laser Melting: A fundamental alloy design approach. Acta Mater 94:59–68 . doi: 10.1016/j.actamat.2015.04.035
6. Kruth JP, Froyen L, Van Vaerenbergh J, et al (2004) Selective laser melting of iron-based powder. J Mater Process Technol 149:616–622 . doi: 10.1016/j.jmatprotec.2003.11.051
7. Weller C, Kleer R, Piller FT (2015) Economic implications of 3D printing: Market structure models in light of additive manufacturing revisited. Int J Prod Econ 164:43–56 . doi: 10.1016/j.ijpe.2015.02.020
8. Hole C (2016) Cost and practicality of in-process monitoring for metal Additive Manufacturing. Met AM 2:63–69
9. Tapia G, Elwany A (2014) A Review on Process Monitoring and Control in Metal-Based Additive Manufacturing. J Manuf Sci Eng 136:60801 . doi: 10.1115/1.4028540
10. Everton SK, Hirsch M, Stravroulakis P, et al (2016) Review of in-situ process monitoring and in-situ metrology for metal additive manufacturing. Mater Des 95:431–445 . doi: 10.1016/j.matdes.2016.01.099
11. Craeghs T, Clijsters S, Yasa E, et al (2011) Determination of geometrical factors in Layerwise Laser Melting using optical process monitoring. Opt Lasers Eng 49:1440–1446 . doi: 10.1016/j.optlaseng.2011.06.016
12. Clijsters S, Craeghs T, Buls S, et al (2014) In situ quality control of the selective laser melting process using a high-speed, real-time melt pool monitoring system. Int J Adv Manuf Technol 75:1089–1101 . doi: 10.1007/s00170-014-6214-8
13. Berumen S, Bechmann F, Lindner S, et al (2010) Quality control of laser- and powder bed-based Additive Manufacturing (AM) technologies. Phys Procedia 5:617–622 . doi: 10.1016/j.phpro.2010.08.089
14. Craeghs T, Clijsters S, Kruth J-P, et al (2012) Detection of Process Failures in Layerwise Laser Melting with Optical Process Monitoring. Phys Procedia 39:753–759 . doi: 10.1016/j.phpro.2012.10.097

15. Craeghs T, Clijsters S, Yasa E, Kruth J-P (2011) Online quality control of selective laser melting. Solid Free Fabr Proc 212–226
16. Craeghs T, Bechmann F, Berumen S, Kruth JP (2010) Feedback control of Layerwise Laser Melting using optical sensors. Phys Procedia 5:505–514 . doi: 10.1016/j.phpro.2010.08.078
17. Kanko JA, Sibley AP, Fraser JM (2016) In situ morphology-based defect detection of selective laser melting through inline coherent imaging. J Mater Process Technol 231:488–500 . doi: 10.1016/j.jmatprotec.2015.12.024
18. Neef A, Seyda V, Herzog D, et al (2014) Low coherence interferometry in selective laser melting. Phys Procedia 56:82–89 . doi: 10.1016/j.phpro.2014.08.100
19. Thombansen U, Gatej A, Pereira M (2014) Process observation in fiber laser–based selective laser melting. Opt Eng 54:11008 . doi: 10.1117/1.OE.54.1.011008
20. Kleszczynski S, Jocobsmuhlen J zur, Sehrt JT (2012) Error Detection in Laser Beam Melting Systems by High Resolution Imaging. Twenty Third Annu Int Solid Free Fabr Symp
21. Krauss H, Eschey C, Zaeh MF (2012) Thermography for Monitoring the Selective Laser Melting Process. In: Proceedings of the Solid Freeform Fabrication Symposium. pp 999–1014
22. Furumoto T, Ueda T, Alkahari MR, Hosokawa A (2013) Investigation of laser consolidation process for metal powder by two-color pyrometer and high-speed video camera. CIRP Ann - Manuf Technol 62:223–226 . doi: 10.1016/j.cirp.2013.03.032
23. Yadroitsev I, Krakhmalev P, Yadroitsava I (2014) Selective laser melting of Ti6Al4V alloy for biomedical applications: Temperature monitoring and microstructural evolution. J Alloys Compd 583:404–409 . doi: 10.1016/j.jallcom.2013.08.183
24. Grasso M, Laguzza V, Semeraro Q, Colosimo BM (2016) In-Process Monitoring of Selective Laser Melting: Spatial Detection of Defects Via Image Data Analysis. J Manuf Sci Eng 139:51001 . doi: 10.1115/1.4034715
25. Liu Y, Yang Y, Mai S, et al (2015) Investigation into spatter behavior during selective laser melting of AISI 316L stainless steel powder. Mater Des 87:797–806 . doi: 10.1016/j.matdes.2015.08.086
26. Matthews MJ, Guss G, Khairallah SA, et al (2016) Denudation of metal powder layers in laser powder bed fusion processes. Acta Mater 114:33–42 . doi: 10.1016/j.actamat.2016.05.017
27. Lane B, Whitenton E, Moylan S (2016) Multiple Sensor Detection of Process Phenomena in Laser Powder Bed Fusion. SPIE Commer Sci Sens Imaging 9861:986104–986104 . doi: 10.1117/12.2224390
28. Hirvimäki M, Manninen M, Lehti A, et al (2013) Evaluation of different monitoring methods of laser additive manufacturing of stainless steel. Adv Mater Res 651:812–819 . doi: 10.4028/www.scientific.net/AMR.651.812
29. Furumoto T, Ueda T, Kobayashi N, et al (2009) Study on laser consolidation of metal powder with Yb:fiber laser-Evaluation of line consolidation structure. J Mater Process Technol 209:5973–5980 . doi: 10.1016/j.jmatprotec.2009.07.017
30. Demir AG, Previtali B (2017) Investigation of remelting and preheating in SLM of

18Ni300 maraging steel as corrective and preventive measures for porosity reduction. Int J Adv Manuf Technol 1–13 . doi: 10.1007/s00170-017-0697-z
31. Demir AG, Colombo P, Previtali B (2017) From pulsed to continuous wave emission in SLM with contemporary fiber laser sources: effect of temporal and spatial pulse overlap in part quality. Int J Adv Manuf Technol 91:2701–2714 . doi: 10.1007/s00170-016-9948-7
32. Kaierle S, Abels P, Kratzsch C (2005) Process Monitoring and Control for Laser Materials Processing – An Overview. In: Proceedings of Lasers in Manufacturing 3. pp 101–105
33. Colombo D, Colosimo BM, Previtali B (2013) Comparison of methods for data analysis in the remote monitoring of remote laser welding. Opt Lasers Eng 51:34–46 . doi: 10.1016/j.optlaseng.2012.07.022
34. Spears TG, Gold SA (2016) In-process sensing in selective laser melting (SLM) additive manufacturing. Integr Mater Manuf Innov. doi: 10.1186/s40192-016-0045-4
35. Mumtaz KA, Hopkinson N (2010) Selective Laser Melting of thin wall parts using pulse shaping. J Mater Process Technol 210:279–287 . doi: 10.1016/j.jmatprotec.2009.09.011
36. Oiwa S, Kawahito Y, Katayama S Optical properties of laser induced plasma during high power laser welding. 359–365
37. Wang C-M, Meng X-X, Huang W, et al (2011) Role of side assisting gas on plasma and energy transmission during CO2 laser welding. J Mater Process Technol 211:668–674 . doi: 10.1016/j.jmatprotec.2010.12.001
38. Miyamoto JT, Inoue T (2002) Characterizing keyhole plasma light emission and plasma plume scattering for monitoring 20 kW class laser welding processes Characterizing keyhole plasma light emission and plasma plume scattering for monitoring 20 kW class CO 2 laser welding processes. J Laser Appl 14:146–153 . doi: 10.2351/1.1493763
39. Colombo D, Previtali B (2010) Through Optical Combiner Monitoring of Fiber Laser Processes. Int J Mater Form 3:1123–1126 . doi: 10.1007/s12289-010-0969-8
40. Pedrotti L (2008) Basic Geometrical Optics
41. Yasa E, Kempen K, Kruth J (2010) Microstructure and mechanical properties of Maraging Steel 300 after selective laser melting. Proc 21st Int Solid Free Fabr Symp 383–396
42. Demir AG, Monguzzi L, Previtali B (2017) Selective laser melting of pure Zn with high density for biodegradable implant manufacturing. Addit Manuf 15:20–28 . doi: 10.1016/j.addma.2017.03.004
43. Demir AG, Colombo P, Previtali B (2017) From pulsed to continuous wave emission in SLM with contemporary fiber laser sources: effect of temporal and spatial pulse overlap in part quality. Int J Adv Manuf Technol. doi: 10.1007/s00170-016-9948-7
44. Demir AG, Pangovski K, O'Neill W, Previtali B (2015) Investigation of pulse shape characteristics on the laser ablation dynamics of TiN coatings in the ns regime. J Phys D Appl Phys 48:235202 . doi: 10.1088/0022-3727/48/23/235202

45. Spierings AB, Levy G (2009) Comparison of density of stainless steel 316L parts produced with selective laser melting using different powder grades. In: Proc. of Solid Freeform Fabrication Symposium. pp 342–353
46. Mcvey RW, Melnychuk RM, Todd JA, Martukanitz RP (2007) Absorption of laser irradiation in a porous powder layer. J Laser Appl 19:214–224 . doi: 10.2351/1.2756854
47. Bi G, Gasser A, Wissenbach K, et al (2006) Characterization of the process control for the direct laser metallic powder deposition. Surf Coatings Technol 201:2676–2683 . doi: 10.1016/j.surfcoat.2006.05.006
48. Ferrar B, Mullen L, Jones E, et al (2012) Gas flow effects on selective laser melting (SLM) manufacturing performance. J Mater Process Technol 212:355–364 . doi: 10.1016/j.jmatprotec.2011.09.020
49. Yasa E, Kruth JP (2010) Investigation of laser and process parameters for Selective Laser Erosion. Precis Eng 34:101–112 . doi: 10.1016/j.precisioneng.2009.04.001

Figure Captions List

Fig. 1 a) Generic description of object, image and lens distances in a three-lens configuration. b) Schematic disposition of the implemented optical arrangement in the monitoring module.

Fig. 2 a) Schematic representation of the monitoring module, and b) the implemented system

Fig. 3 Photograph of the realized specimens

Fig. 4 Effect of process parameters on the part porosity

Fig. 5 Example of signal acquired with the laser channel depicting a) volume and remelting passes, b) zoomed signal showing back reflected laser pulses.

Fig. 6 Examples of images and signal acquired with the visible channel depicting a) Melt pool collapse (t_{on}=70 µs, N_l=32, volume pass). b) Signal intensity showing instances of melt pool separation and spark generation (t_{on}=80 µs, N_l=32, volume pass). Images show an area of 1x1 mm^2.

Fig. 7 Example of signal dynamics acquired with the NIR channel depicting change in thermal emission at the remelting pass (N_l=32, soft remelting)

Fig. 8 Mean value of back reflected laser intensity as a function of process parameters

Fig. 9 Mean value of image intensity in the visible bandwidth as a function of process parameters

Fig. 10 Mean value of image intensity in the near infrared bandwidth as a function of process parameters

Fig. 11 a) Change in mean intensity of visible channel at volume pass over different layer as a function of total energy. b) Relationship between visible mean intensity and porosity. The dashed lines are for visualizing the trend only.

Table Caption List

Table 1 Physical phenomenon related to defect formation and related sensor parameters

Table 2 Main characteristics of the flexible SLM prototype Powderful

Table 3 Final dimensions of the implemented monitoring module for Vis and NIR channels in order to obtain 1x1 mm^2 field of view.

Table 4 Details of the experimental plan

Table 5 Parameters of the remelting strategies

Figures

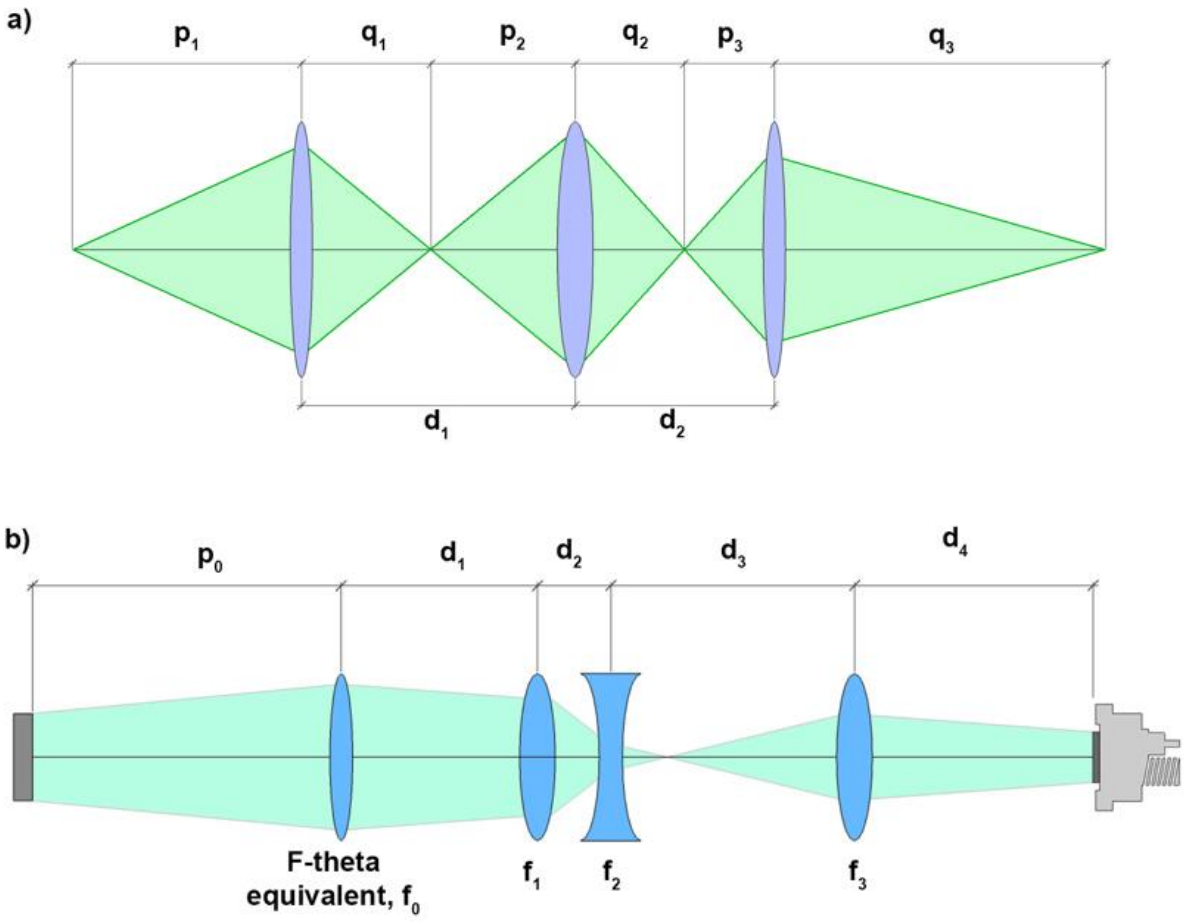

Figure 1.

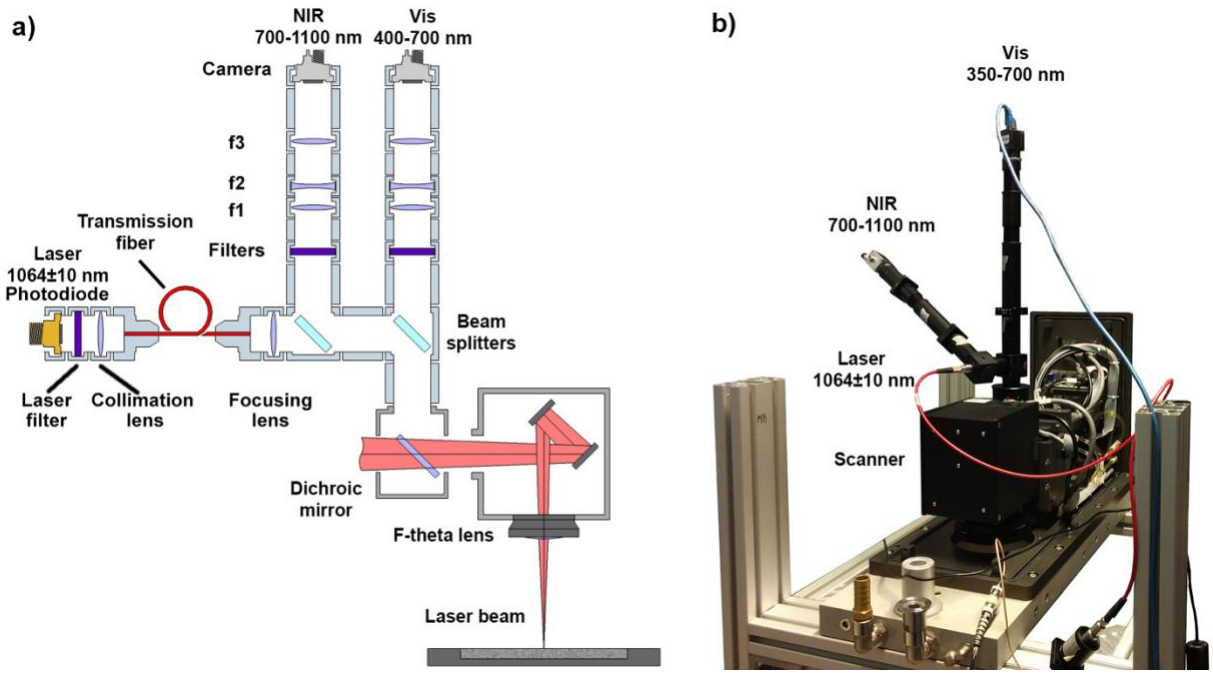
a)
NIR
700-1100 nm
Vis
400-700 nm
Camera
f3
f2
f1
Transmission
fiber
Filters
Laser
1064±10 nm
Photodiode
Beam
splitters
Laser
filter
Collimation
lens
Focusing
lens
Dichroic
mirror
F-theta lens
Laser beam
b)
Vis
350-700 nm
NIR
700-1100 nm
Laser
1064±10 nm
Scanner

Figure 2.

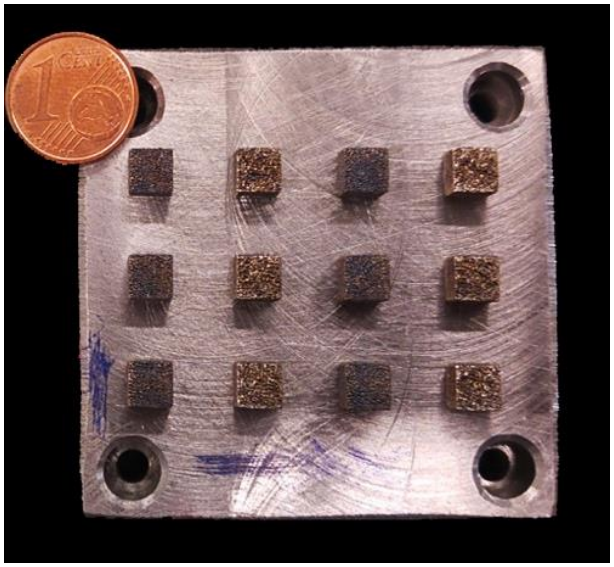

Figure 3.

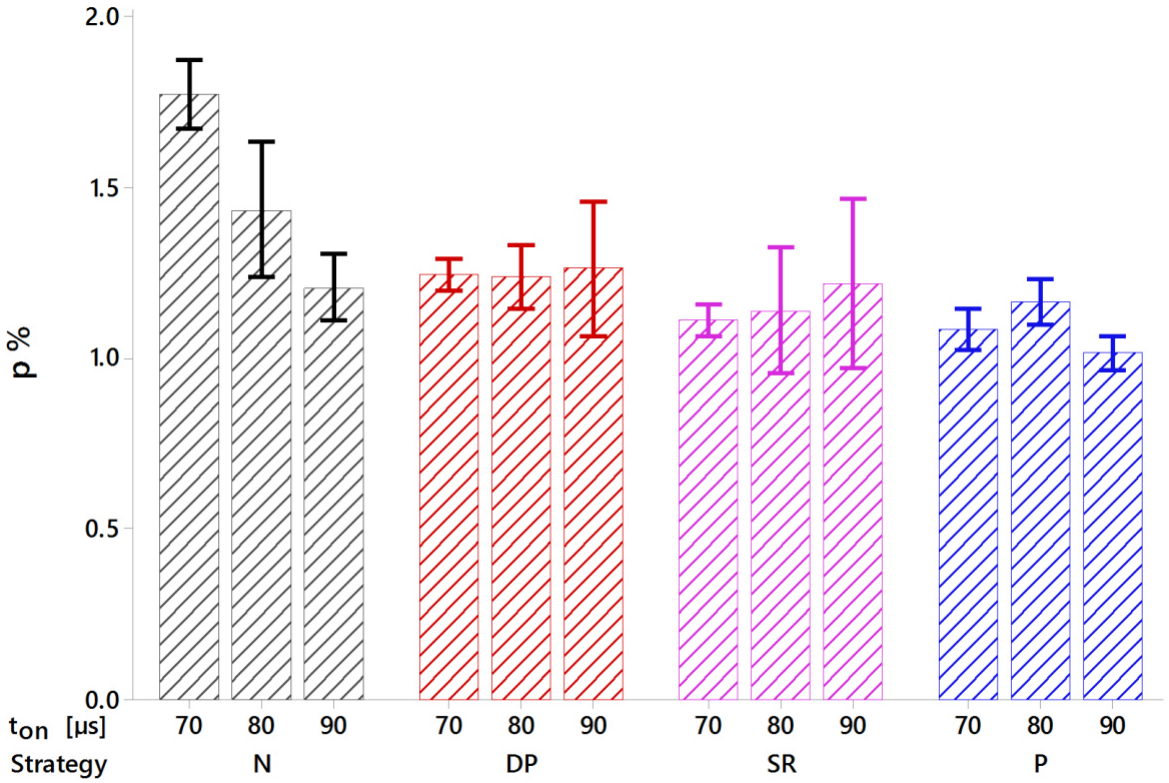
2.0
1.5
1.0
0.5
0.0
p %
ton [µs]
70
80
90
70
80
90
70
80
90
70
80
90
Strategy
N
DP
SR
P

Figure 4.

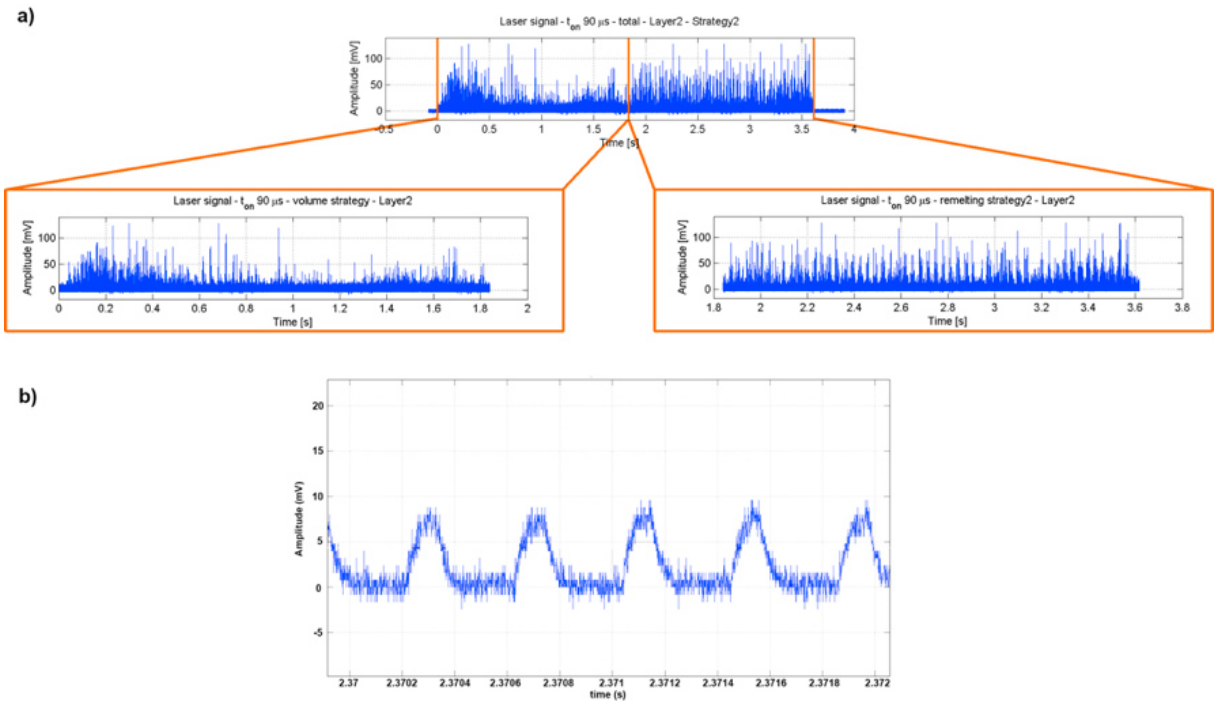
a)
Laser signal - t_{on} 90 µs - total - Layer2 - Strategy2
Amplitude [mV]
Time [s]
Laser signal - t_{on} 90 µs - volume strategy - Layer2
Amplitude [mV]
Time [s]
Laser signal - t_{on} 90 µs - remelting strategy2 - Layer2
Amplitude [mV]
Time [s]
b)
Amplitude (mV)
time (s)

Figure 5.

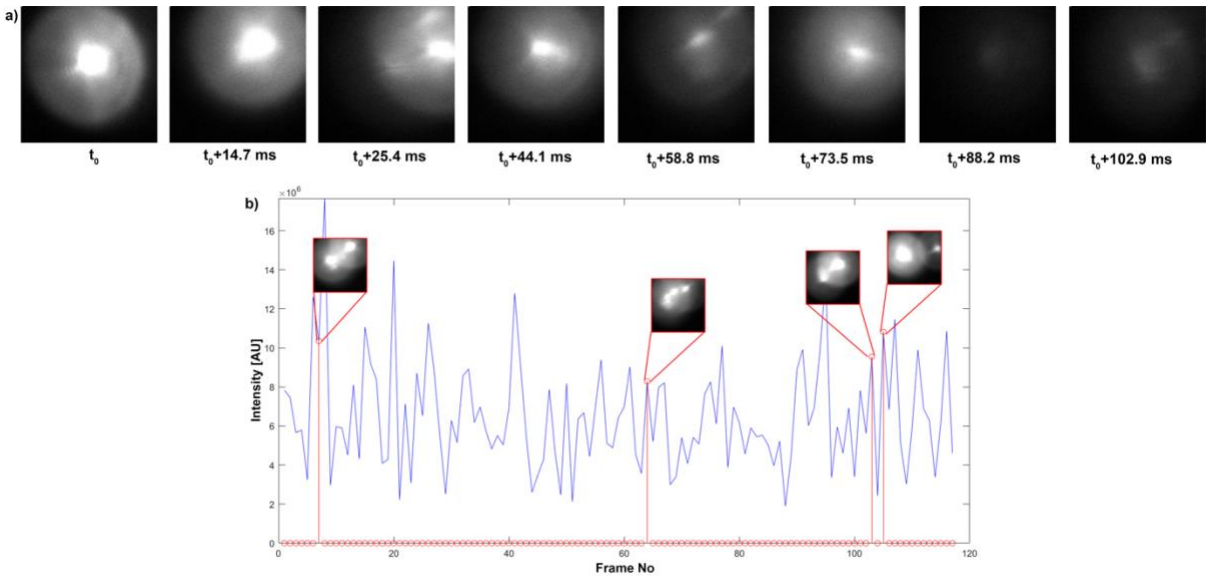
a)
t_0
t_0+14.7 ms
t_0+25.4 ms
t_0+44.1 ms
t_0+58.8 ms
t_0+73.5 ms
t_0+88.2 ms
t_0+102.9 ms
b)
×10^6
Intensity [AU]
Frame No

Figure 6.

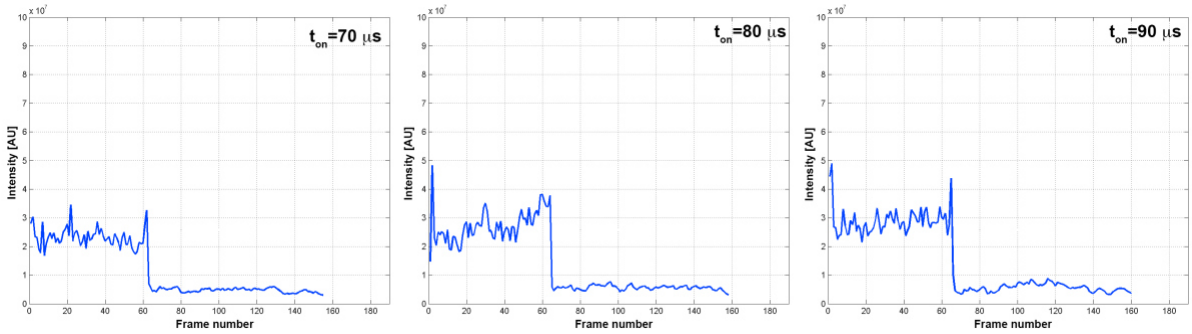

Figure 7.

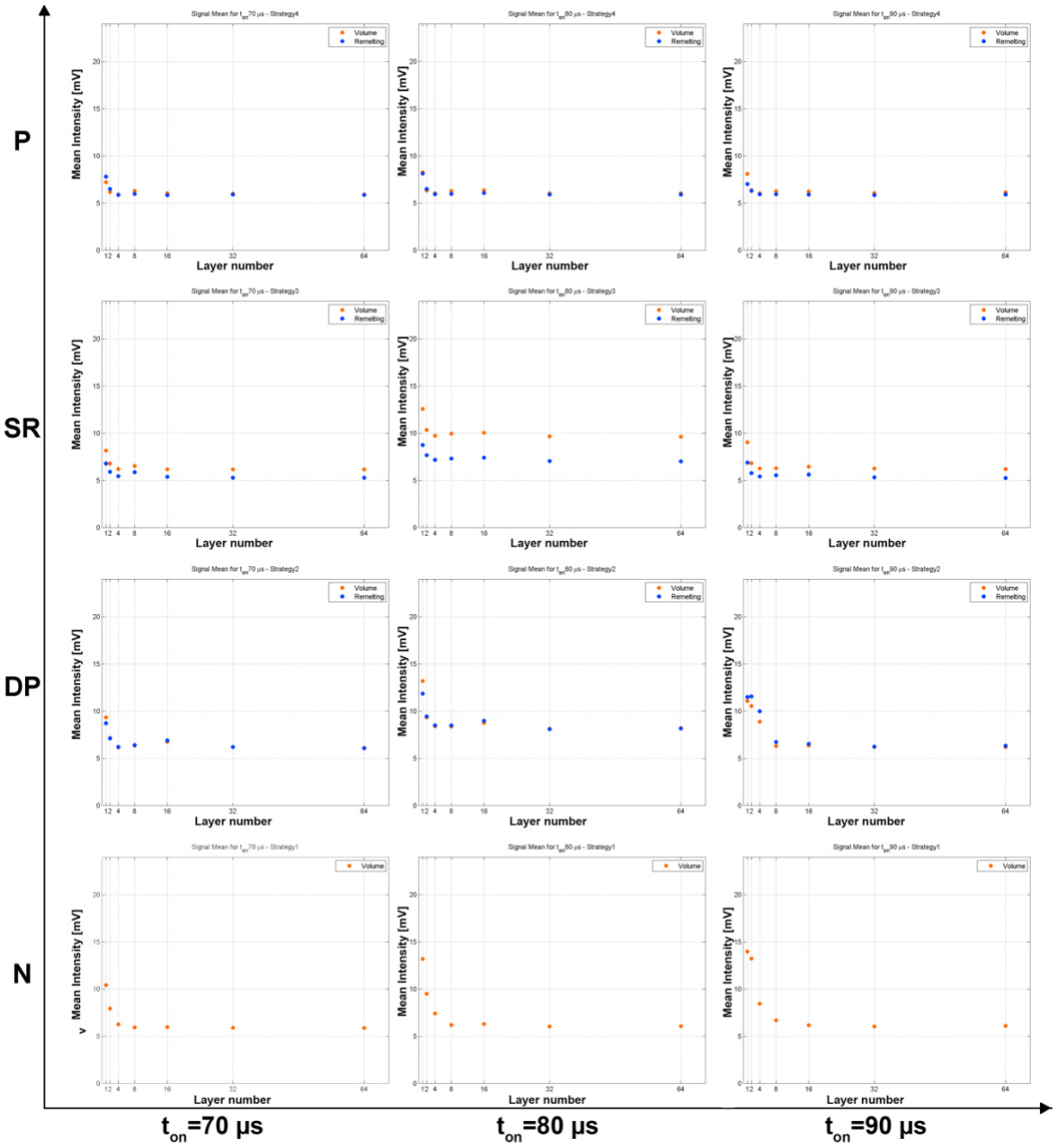
P
SR
DP
N
Mean Intensity [mV]
Layer number
Volume
Remelting
t_on=70 µs
t_on=80 µs
t_on=90 µs

Figure 8.

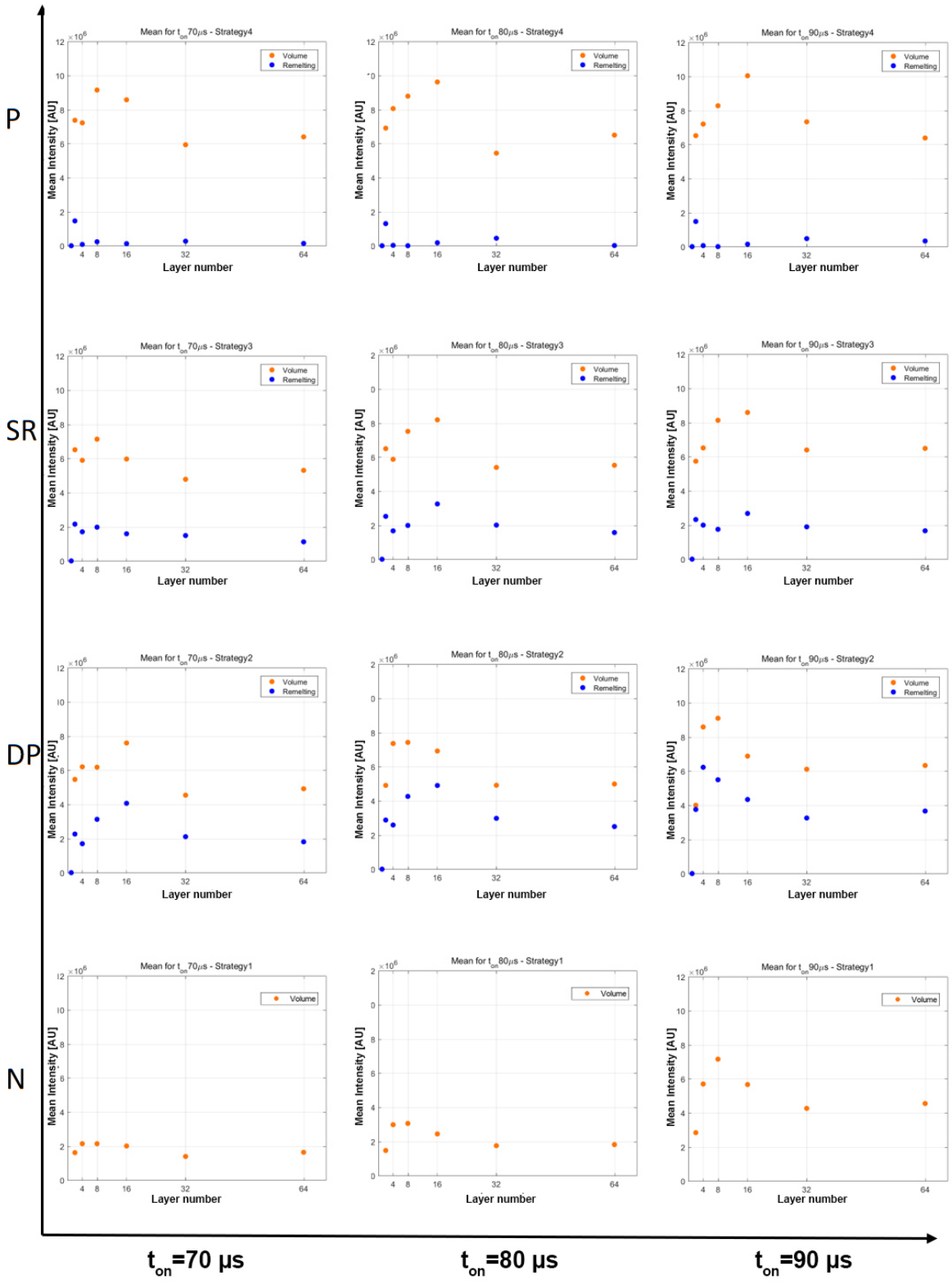
P
SR
DP
N
Mean for t_on 70μs - Strategy4
Mean for t_on 80μs - Strategy4
Mean for t_on 90μs - Strategy4
Mean for t_on 70μs - Strategy3
Mean for t_on 80μs - Strategy3
Mean for t_on 90μs - Strategy3
Mean for t_on 70μs - Strategy2
Mean for t_on 80μs - Strategy2
Mean for t_on 90μs - Strategy2
Mean for t_on 70μs - Strategy1
Mean for t_on 80μs - Strategy1
Mean for t_on 90μs - Strategy1
Volume
Remelting
Mean Intensity [AU]
Layer number
t_on=70 μs
t_on=80 μs
t_on=90 μs

Figure 9.

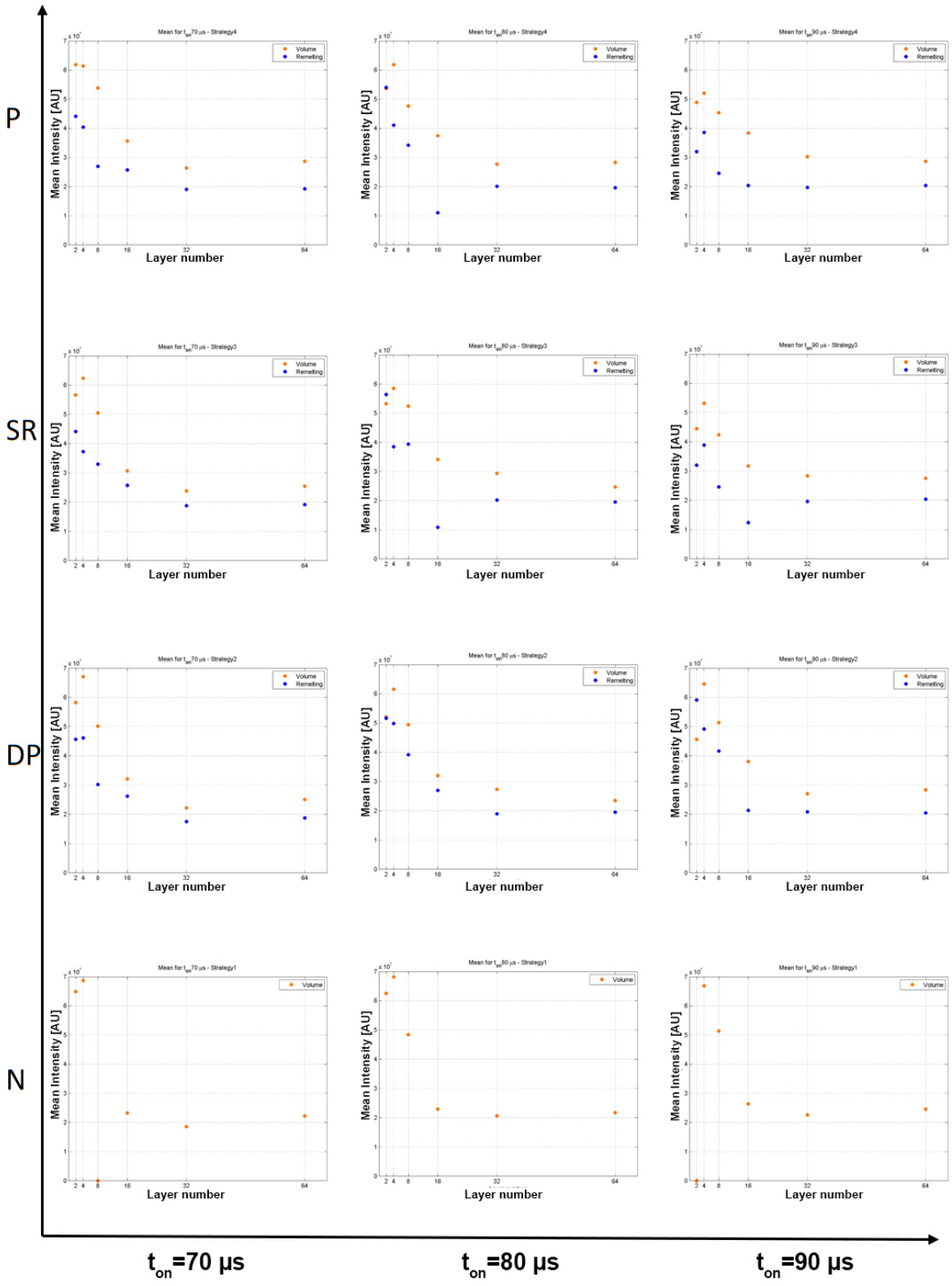
P
SR
DP
N
Mean Intensity [AU]
Layer number
Volume
Remelting
t_{on}=70 µs
t_{on}=80 µs
t_{on}=90 µs

Figure 10.

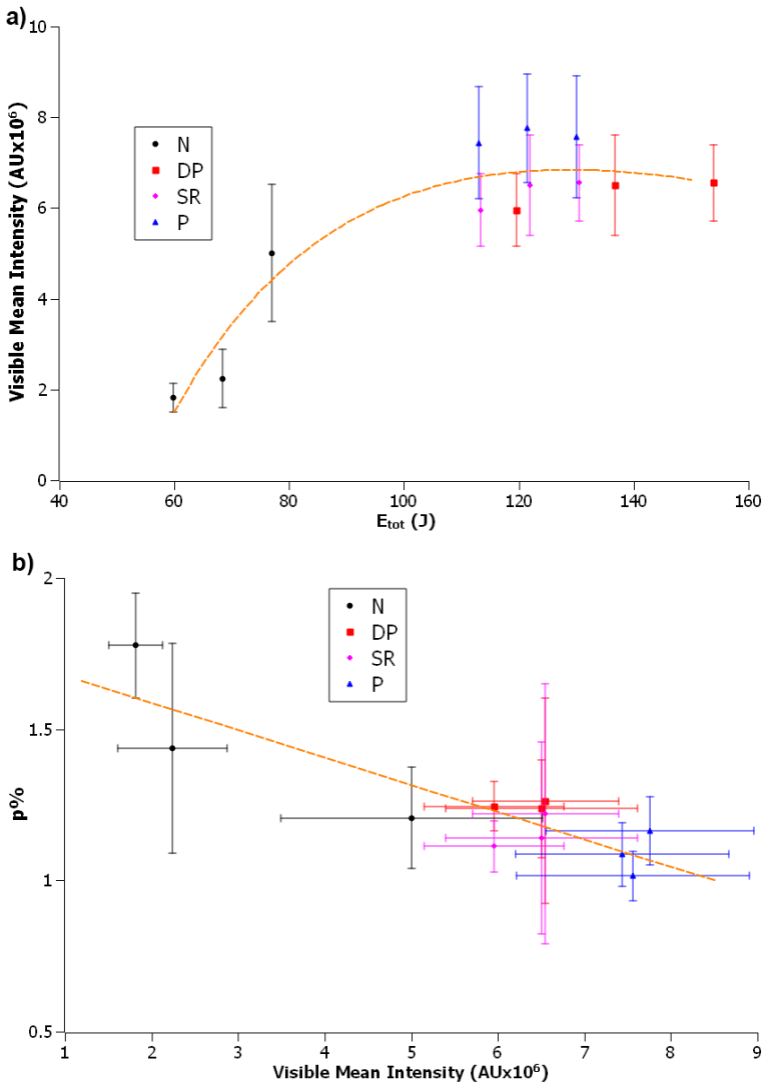
a)
Visible Mean Intensity (AUx10⁶)
E_tot (J)
N
DP
SR
P
b)
p%
Visible Mean Intensity (AUx10⁶)
N
DP
SR
P

Figure 11.

Tables

Table 1.

Phenomenon	Physical reference	Wavelength band	Temporal scale	Spatial scale
Laser absorption	Pulse duration, spot diameter	Same as the laser	50-500 µs	30-200 µm
Porosity formation	Layer thickness, hatch and spot distance, plasma	Near UV - Vis	100-1000 µs	50-500 µm
Thermal gradient	Layer number, molten pool, thermal radiation	NIR	>1 s	>500 µm

Table 2.

Parameter	**Value**
Laser emission wavelength, λ	1070 nm
Max. laser power, P_{max}	250 W
Beam quality factor, M^2	1.1
Nominal beam diameter on focal plane, d_0	60 µm
Build platform area (DxWxH)	60x60x20 mm^3

Table 3.

Parameter	Vis	NIR
d_{sensor} (mm)	1.2	1.2
m_{tot}	1.2	1.2
p_0 (mm)	207	207
d_1 (mm)	585	650
d_2 (mm)	20	20
f_0 (mm)	386	386
f_1 (mm)	50	50
f_2 (mm)	-50	-50
f_3 (mm)	25	25
d_3 (mm)	124.8	125.7
d_4 (mm)	120.3	96.2

Table 4.

Fixed parameters	
Laser peak power, P_{peak} (W)	200
Point distance, d_p (μm)	65
Hatch distance, d_h (μm)	90
Focal position, Δz (mm)	0
Layer thickness, z (μm)	40
Varied parameters	
Pulse duration, t_{on} (μs)	70, 80, 90
Remelting strategy	None, Polishing (*P*), Soft remelting (*SR*), Double pass (*DP*)

Table 5.

Strategy	P_{peak}(W)	t_{on} (μs)	d_p (μm)	d_h (μm)	f (mm)	E_{tot} (J)		
						t_{on}=70 μs	t_{on}=80 μs	t_{on}=90 μs
Polishing, *P*	200	85	80	100	-2	113	121	130
Soft remelting, *SR*	150	50	35	100	0	113	122	131
Double pass, *DP*	200		Same as the first pass			120	138	154
None, *N*			None			60	69	77

Table 6.

Strategy	*BR* (cm^3/h)		
	t_{on}=70 µs	t_{on}=80 µs	t_{on}=90 µs
Polishing, *P*	6.4	5.9	5.5
Soft remelting, *SR*	5.5	5.2	4.9
Double pass, *DP*	6.2	5.3	4.7
None, *N*	12.0	10.5	9.4